HHS Public Access

Author manuscript

IEEE Robot Autom Lett. Author manuscript; available in PMC 2018 July 01.

Published in final edited form as:

IEEE Robot Autom Lett. 2017 July ; 2(3): 1625–1631. doi:10.1109/lra.2017.2678543.

Development and Experimental Evaluation of Concurrent Control of a Robotic Arm and Continuum Manipulator for Osteolytic Lesion Treatment

Paul Wilkening [Member, IEEE],
Department of computer Science, Johns Hopkins university, Baltimore, MD uSA

Farshid Alambeigi [Member, IEEE],
Department of Mechanical Engineering, Johns Hopkins university, Baltimore, MD, uSA

Ryan J. Murphy [Member, IEEE],
Research and Exploratory Development Department, Johns Hopkins university Applied Physics Laboratory, Laurel, MD, uSA

Russell H. Taylor [Life Fellow, IEEE], and
Department of computer Science, Johns Hopkins university, Baltimore, MD uSA

Mehran Armand [Member, IEEE]
Department of Mechanical Engineering, Johns Hopkins university, Baltimore, MD, uSA

Research and Exploratory Development Department, Johns Hopkins university Applied Physics Laboratory, Laurel, MD, uSA

Abstract

This paper presents the development and evaluation of concurrent control of a robotic system for less-invasive treatment of osteolytic lesions behind an acetabular implant. This system implements safety constraints including a remote center of motion (RCM), virtual walls, and joint limits while operating through the screw holes of the acetabular implant. The formulated linear constrained optimization problem ensures these constraints are satisfied while maintaining precise control of the tip of a Continuum Dexterous Manipulator (CDM) attached to a positioning robot. Experiments evaluated the performance of the tip control method within an acetabular cup. The controller reliably reached a series of goal points with a mean error of 0.42 mm and a worst-case error of straying 1.0 mm from our path.

Index Terms

Dexterous manipulation; medical robots and systems; optimization and optimal control

I. Introduction

We have developed a continuum dexterous manipulator [1, 2] (cDM) for use in orthopaedic applications, with a focus on treating osteolysis due to polyethylene liner wear during hip revision surgery [3–5]. The less-invasive treatment of osteolysis involves the manipulation of instruments through the screw holes of a well-fixed acetabular cup component. The surgeon

can remove a larger amount of the lesion through the use of the cDM with flexible tools [6–9] that are fed through its instrument channel, because of their high degree of dexterity [10] as shown in Figure 1.

The CDM may be paired with a robotic arm to ensure precise entry into the acetabular cup's screw hole. A typical osteolytic lesion removal procedure using our CDM device will begin by passing a flexible surgical drill through the instrument channel, and excavating the majority of the lesion pre-operatively identified via a preoperative CT scan through the screw hole. After this is complete, the drill will be removed and a flexible orthopedic bone curette will be mounted to the CDM. The surgeon will then scrape away the remaining lesion, ensuring all lesion material inside of this cavity is loose. This material will be removed via a surgical suction pump. Surgeons will tele-operate the CDM to control its motion and that of the attached tools. Motions of the robot and CDM will be calculated using constrained optimization techniques to properly follow the surgeon's commanded CDM tip velocity while enacting a series of virtual fixtures [11], or safety constraints on robotic motion. While guiding the CDM, the surgeon will receive visual feedback of the CDM within the hip interior and force feedback from the haptic device. Fiber Bragg grating (FBG) sensors inserted into holes running the length of the CDM wall will allow visualization of the CDM within the lesion cavity by providing shape-sensing functionality, and the haptic device will gently guide the surgeon to avoid unsafe movements based on the optimization output. By guiding the surgeon's movements of the robot and CDM with virtual fixtures in this manner, the osteolytic lesion treatment process can be made both safer and more effective.

The use of concurrent control between a robotic arm and CDM has been proposed for other medical applications such as minimally-invasive throat procedures [12, 13]. This work, however, is novel in the CDM used, its kinematic model, and our targeted surgical application. The CDM used [1, 2] was developed by our group and so is unique to our work. This CDM is designed as two nested nitinol tubes with notches removed from the sides as shown in Figure 1, whereas the CDM used in the work cited above is composed as a multibackbone unit [12, 13]. As the construction of this CDM is unique, a new kinematics model [14] was developed to precisely control its motions. The use of the concurrent control of a robot arm and CDM is also novel within the osteolysis treatment application, which necessitates a set of safety constraints different from other applications. There has been preliminary work with this proposed setup [15], but these tests only used a simulation with a simpler set of constraints that did not avoid collisions of the robotic arm or CDM. Manual control of the CDM within a workspace as enclosed as an osteolytic lesion is a challenging task, due to limited visibility of the CDM workspace and the amount of surgeon's manual interaction needed to control both the CDM and the tool passing through it; therefore, the guidance offered by the additional virtual fixtures in this work are essential for properly taking advantage of the high dexterity capable of the CDM. Using a physical setup instead of the aforementioned simulation also shows that our system can handle errors in the robot and CDM control.

We seek to evaluate the performance of our concurrent control of the CDM and robotic arm by having the CDM tip follow a predetermined path behind an acetabular cup. We aim to

show that we can closely follow an arbitrary path with the CDM within its workspace behind the acetabular cup without violating any of a series of safety constraints. Safely following a path in this manner demonstrates that our system may be precise enough for clinical applications. Section II outlines our future plans for a robotic system for osteolytic lesion removal and section III explains the calculation of the kinematics of the coupled UR5 and CDM. Section IV describes the calibration experiments performed to relate the acetabular cup and goal points to robot coordinates, and section V shows the mathematical formulation of the virtual fixtures used to guide and constrain the motion of the CDM and robotic arm. Section VI gives details on the experiment evaluated in this paper, and section VII analyzes the results of this experiment and its significance. In section VIII, we show the areas of our experiment that need improvement and our next steps towards clinical applications.

II. Kinematics

For proper concurrent control of the UR5 and CDM, kinematics of the combined system needs to be defined. Forward kinematics and Jacobian functions of the combined system are calculated using the individual kinematics of the UR5 and cDM.

A. Positioning Robot

The robot arm selected for this experiment was the UR5 (Universal Robots, Inc., Odense, Denmark). It has been used in a multitude of other applications and shown to place its end effector with a precision of 0.1 mm [16]. It also has a tooling plate that supports mounting a custom actuator (Figure 3) used to control the cDM.

The kinematics of the UR5 is defined by a series of 6 revolute joints. The frame of the UR5 end effector is given by a function of the current joint positions $F_{UR5}(q_{UR5})$ determined using the Denavit-Hartenberg convention. The Jacobian function for the UR5, J_{UR5}, defines the relationship between joint velocities of the UR5, $\dot{q}_{UR5}$, and the velocity of the end effector in Cartesian space, $\dot{x}_{EE}$, as

$$J_{\mathrm{UR}5}(q_{\mathrm{UR}5}) * \dot{q}_{\mathrm{UR}5} = \dot{x}_{\mathrm{EE}}.$$

B. CDM

The CDM's design [1,2] consists of a superelastic nitinol tube with alternating notches on two sides and an instrument channel. The notches are positioned to allow bending along a single plane (Figure 1). Stainless steel cables are threaded through channels in two opposing sides of the CDM wall and tied off at the end of the manipulator. Pulling these cables controls the shape of the CDM along its bending plane.

We previously performed an experiment in free space [10] which calculated Bernstein polynomials that relate the cable length of the CDM and its tip position. Taking x to be the CDM's bending direction, we have the functions

$$p_{\mathrm{CDM},x} = B_n(l)$$

$$p_{\mathrm{CDM},z}=\sum_{i=1}^{3}a_i\sin(b_i p_{\mathrm{CDM},x}+c_i).$$

Here $p_{CDM,x}$ and $p_{CDM,z}$ are the x and z components of the CDM tip position relative to its base (Figure 1), l is the cable length of the CDM, B_n represents an nth order Bernstein polynomial, and a, b, c are parameters of the sinusoid that fit the x component of the CDM tip position to its z component. Differentiating this function gives us the velocity of the CDM tip. The CDM Jacobian becomes

$$J_{\mathrm{CDM}}(l)=\frac{\mathrm{dp}_{\mathrm{CDM}}(l)/\mathrm{dl}}{\mathrm{dl}/\mathrm{dt}}$$

This Jacobian function was constructed based on the results of a series of experiments performed in free space [10], so it may not be reliable for shapes of the CDM that are the result of contact forces. Nonetheless, this is representative of a real scenario where our Jacobian may only be reliable for “direction”. For example, repeatedly bending CDM cables may alter the friction between the CDM interior and the cable or cause plastic deformation in the cable, and inaccuracies in the manufacturing process of the CDM may change its properties. These differences in the CDM configuration introduce a noticeable error term in this Jacobian function, but we hypothesize the Jacobian is still functional enough to guide the CDM tip in the direction of its destination. Thus, the addition of real-time feedback on the CDM tip location is able to correct any remaining errors in our CDM shape estimation.

C. Coupled UR5 and CDM

The separate kinematics of the UR5 and CDM are then combined into a form that can be used in a constrained optimization framework: the CDM tip location relative to the UR5 base and a combined Jacobian. The frame of the CDM tip relative to the UR5 base is defined as

$$F_{\mathrm{Combined}}(q)=F_{\mathrm{UR5}}(q_{\mathrm{UR5}})*F_{\mathrm{Base}}*p_{\mathrm{CDM}}.$$

F_{Base} is the transformation between the UR5 end effector and the base of the snake, and it remains constant. This transformation will be calculated during the calibration step. The Jacobian of the CDM tip when paired with the UR5 is defined as

$$J_{\mathrm{Combined}}(q)=[J_{\mathrm{UR5}}(q)\quad J_{\mathrm{CDM}}(q)];J_{\mathrm{Combined}}(q)\in\mathbb{R}^{6\times 7}.$$

Note that q is defined as

$$q=[q_{\mathrm{UR5}}\quad l];q\in\mathbb{R}^{7}.$$

III. CDM Tip Tracking and Control

In the surgical scenario outlined in section I, FBGs [17–19] will be used for real time closed-loop control and occasional x-ray images [20] will be taken to correct for errors and reconfirm relation of the snake to the anatomy. Since real-time sensing with FBGs was still under investigation during this work, we chose to instead track an optical marker mounted to the tip of the CDM using a Polaris optical tracker (Northern Digital Inc., Waterloo, Canada). The use of an optical tracker requires line-of-sight between the tracker and markers and so would not be useful in clinical applications, but our ultimate plan of using x-ray imaging and/or FBGs instead solves this issue. For the CDM tip to follow a path closely, we calculated the next movement of the UR5 and CDM together using constrained optimization techniques. The constraints used in the optimization process prevent collisions or other unsafe movements, ensuring that the relationship between cable lengths and CDM shapes match those measured during free-bending tests (i.e., bending the manipulator without any external force) as closely as possible.

IV. Calibration

Concurrent control of the CDM tip with a robot arm is only possible with knowledge of the relationship between the robot and CDM coordinates. Similarly, the CDM cannot be navigated within the acetabular cup without first calculating the transformation between the coordinate system of its tip and that of the robot. Several preliminary experiments were performed to calculate these transformations using a Polaris optical tracker. The Polaris is able to achieve a RMS error of 0.35 mm [21]. We have constructed several Polaris tools for use with this system, including a reference body. To avoid maintaining a fixed relationship between the tracker and other objects in the experimental setup, all tracker measurements are defined in the coordinates of a fixed, global reference body attached to the base of the table (Figure 3).

A. CDM Tip Calibration

To properly understand the translational and rotational offset between the robot's end effector and the CDM tip (F_{Base}), a calibration jig was designed (4A). If the jig is inserted fully into the CDM's instrument channel, the CDM tip frame will be located at the origin of the calibration jig, with its z-axis aligned with that of the UR5 end effector frame. This means that a "hand-eye" [22] calibration between the robot and tracker performed with this calibration jig inserted into the CDM defines the value of F_{Base} for the actuation unit. Using this value of F_{Base}, we can derive the fixed transformation between tracker coordinates and robot coordinates F_{TR} as

$$F_{\mathrm{TR}} = {F_{\mathrm{UR}5}}^{-1} * F_{\mathrm{Base}} * F_{\mathrm{Tracker}}.$$

$F_{Tracker}$ is the location of the calibration jig with respect to the tracker reference tool given a pose of the UR5 end effector F_{UR5}. This transformation allows us to relate the locations of the Polaris tools in further tests to the robot's coordinate frame.

B. Acetabular Cup Digitization

We manufactured a digitizer (Figure 4B) specifically for locating the center of a screw hole in the acetabular cup. Instead of tapering to a point, the tip of the digitizer's rod ends in a sphere with a 5 mm radius, capable of fitting in the acetabular cup used for the experiment. Once inserted, a pivot calibration [23] is performed with readings from the Polaris to find the optimal RCM point p_{RCM}. Once the CDM tip calibration is performed as outlined in the previous section, we can easily relate this RCM point to robot base coordinates (Figure 2).

V. Constrained Optimization Control

For a concurrent control of the robotic arm and CDM, we used a constrained optimization framework [11] that periodically calculates the next incremental movement of a robot by minimizing a series of linear objective functions in a way that does not violate any of its constraints. The general form of this optimization problem is:

$$\mathrm{argmin}_{\mathrm{dq}} \left| |M_{\mathrm{Obj}} * \mathrm{dq} - \nu_{\mathrm{Obj}}| \right|^2$$

s.t.

$$M_{\mathrm{Ineq}} * \mathrm{dq} \geq \nu_{\mathrm{Ineq}}; M_{\mathrm{Eq}} * \mathrm{dq} = \nu_{\mathrm{Eq}}$$

Where M denotes an n_ν by n_q matrix, where n_ν is the number of rows (as long as we have some objective), n_q is the number of "joints" for the system ($n_q = 7$), and ν denotes a vector of length n_ν. The "Obj", "Ineq", and "Eq" labels refer to the optimization problem's objective, inequality constraint expression, and equality constraint expression respectively. Note that each term listed here can have multiple entries.

The control algorithm uses this framework to compute motions of the UR5 and CDM as follows:

1. Query the UR5 and CDM for the current joint values and cable length measurement.
2. Using the combined kinematics model of the UR5 and CDM as discussed in section II [15] and the values of F_{Base} and p_{RCM} from the calibration tests in section III, calculate the position and orientation of the CDM tip $F_{Combined}$. If we see error between the location of $F_{Combined}$ and the CDM tip marker, correct the translational term of $F_{Combined}$ so that it matches the location of the marker.
3. Calculate the desired incremental motion of the CDM tip in Cartesian space dx based on the difference between the current CDM tip position and the next point on the goal path.
4. Solve the constrained optimization problem outlined in the following sections that minimizes the difference between the calculated incremental motion and the desired incremental motion while satisfying all constraints.

5. Send joint velocities to the UR5 and a new cable length to the CDM according to the values returned by the constrained optimization solver. The magnitude of this movement is limited by velocity limits and the period of the control algorithm loop.
6. Check the proximity of the CDM tip marker to the next goal position. If it is within an acceptable distance (set to 1 mm for this experiment), change our desired position to the next point in the path.
7. Repeat from step 1.

A. Objective Function

Our objective function minimizes the difference between the desired incremental motion in Cartesian space of the CDM tip and the motion produced by the next value of the commanded incremental joint motions and the change of cable length. This is given by the formula

$$\mathrm{argmin}_{\mathrm{dq}}||J_{\mathrm{combined}} * \mathrm{dq} - \mathrm{dx}_{\mathrm{obj}}||^2.$$

As $J_{Combined}$ was calculated using experiments without collisions, the entire CDM must be within the acetabular cup and there must be no collisions for this Jacobian to still be valid. dq is the next incremental joint motion, and is the set of variables we are solving for in the above equation. As in the q vector, the first six values of dq represent the change in position of the six joints of the UR5, and the seventh value represents the change in cable length for the CDM. If dx is defined to be the Cartesian vector calculated from the CDM tip position to the next desired goal position in the path, then dx_{obj} is defined as:

$$\mathrm{dx}_{\mathrm{obj}} = k_p \mathrm{dx} + k_d \frac{\mathrm{dx}}{\mathrm{dt}}$$

Here, we are using two gain terms: a proportional term k_p and a derivative term k_d. These gains are used in the objective to calculate a Cartesian movement that will minimize the magnitude of dx as quickly as possible. This ensures that the CDM tip will closely follow the path without oscillating. The combined Jacobian allows us to solve directly for incremental joint values that best match the desired motion of the CDM without violating any of the following constraints.

B. Joint Limit Constraints

The joint velocity limits are as follows

$$\mathrm{dq} \geq \mathrm{dq}_{\mathrm{Lower}}; -\mathrm{dq} \geq -\mathrm{dq}_{\mathrm{Upper}}$$

Here dq_{Lower} and dq_{Upper} refer to the lower and upper incremental joint position limits, respectively. This ensures that the incremental joint values will not be above or below given thresholds, and therefore that the UR5 or CDM will not move above a safe and steady

velocity. Given safe upper and lower velocity limits $\dot{q}_{Lower}$ and $\dot{q}_{Upper}$ and the time between calls to the optimizer dt, the corresponding limits on the incremental joint movement are

$$\mathrm{dq}_{\mathrm{Upper}}=\dot{q}_{\mathrm{Upper}}\mathrm{dt};\mathrm{dq}_{\mathrm{Lower}}=\dot{q}_{\mathrm{Lower}}\mathrm{dt}$$

Similarly, the joint position limits are as follows

$$\mathrm{dq}\geq q_{\mathrm{Lower}}-q;-\mathrm{dq}\geq -q_{\mathrm{Upper}}+q$$

q is the vector of current joint values, and q_{Lower} and q_{Upper} are the bounds on the joint values specified by the UR5 hardware and CDM kinematics. The UR5 is composed of revolute joints, each with a range from −360 degrees to 360 degrees. The CDM has an effective range of 0 mm of the cable pulled out of the CDM to 18 mm of the cable pulled. This was the range of cable tensions used to calculate the Jacobian used in the objective function, and therefore we must be sure to keep the CDM within these bounds in order for the Jacobian to be reliable. This represents a rotation of the CDM tip by approximately 180 degrees.

C. RCM Constraint

This RCM constraint [11] ensures that the magnitude of Δx_c, the movement of the closest point on the UR5's shaft axis to a given point p_{RCM}, cannot be larger than a specified distance ε. p_{RCM} is chosen as the center of the screw hole in the acetabular cup, ensuring that the base of the CDM avoids contact with the sides of the screw hole by pivoting about p_{RCM}. The formulation of this constraint is given by

$$H*J_{\mathrm{Closest}}*\mathrm{dq}_{\mathrm{UR5}}\geq h$$

$J_{Closest}$ is the UR5's Jacobian resolved at the closest point on its shaft axis to the RCM point and dq_{UR5} is the next movement of the UR5 without a change in the CDM cable tension. We restrict the variables being calculated to purely UR5 joint values to ensure that we do not change the shape of the CDM with a constraint that should not have any influence on it. H and h are a matrix and vector determined by a cylinder created around the shaft axis of the UR5. If a cylinder is approximated by a collection of planes (Figure), with plane normals ν_1 through ν_n, we define our RCM variables

$$H=\begin{bmatrix}\nu_1\\ \vdots\\ \nu_n\end{bmatrix}$$

$$h=\begin{bmatrix}\varepsilon+\nu_1*(p_{\mathrm{RCM}}-p_{\mathrm{Closest}})\\ \cdots\\ \varepsilon+\nu_2*(p_{\mathrm{RCM}}-p_{\mathrm{Closest}})\end{bmatrix}.$$

$p_{Closest}$ is defined as the closest point on the UR5 shaft axis to the RCM point.

D. Stay Near Axis Constraint

Although the RCM is able to restrict the closest point on the UR5 shaft axis to the center of the screw hole of the acetabular cup, it is also necessary to restrict the axis of entry to the cup. If this axis is not close enough to what is considered ideal, collisions could occur with the sides of the screw holes. This constraint is enforced using the equation

$$\mathrm{axis}^{T}{}_{\mathrm{des}} * J_{\mathrm{Base}} * \mathrm{dq} \geq \cos(\theta_{\mathrm{tol}}) - \mathrm{axis}_{\mathrm{des}} * \mathrm{axis}_{\mathrm{cur}}$$

$axis_{des}$ is an ideal axis value for the UR5 shaft for entry into the screw hole without collisions and $axis_{cur}$ is the current shaft axis of the UR5. J_{Base} is the Jacobian of the UR5 resolved at the CDM base, and θ_{tol} is the maximum allowable angle between the ideal axis and the next shaft axis of the UR5.

E. Virtual Wall Constraint

A virtual wall is a plane that we forbid the CDM base from crossing to avoid collisions that are due to the bend of the CDM. Although the underside of the osteolytic cup is free from obstacles, we must ensure that the entire CDM is within the cup to avoid collisions with the sides of the screw holes. As previously stated, our Jacobian function J_{CDM} does not allow for any collisions of the CDM body so this is a necessary constraint for our estimation of the CDM tip to be precise. This constraint restricts the CDM base from crossing a plane that runs perpendicular to the desired entry axis of the screw hole as shown in Figure . The formulation for this constraint is given as

$$n^{T} * J_{\mathrm{Base}} * \mathrm{dq} \geq e - n^{T} * p_{\mathrm{Base}}$$

Here n^T is the transpose of the normal vector of this plane, J_{Base} is again the Jacobian at the base of the CDM, and p_{Base} is the position of the base of the CDM in robot coordinates. e is defined as the constant in the standard plane equation

$$e = \mathrm{ax} + \mathrm{by} + \mathrm{cz}$$

Where x, y, and z are defined as the components of the position of the CDM base.

VI. Experiment

To evaluate the precision of our concurrent control of the UR5 and CDM, we attempted to get the CDM tip to follow a path. For this test, the CDM was mounted onto the actuation unit and inserted into the acetabular cup as shown in Figure 8. We chose a value of 1 mm for the maximum allowable distance the marker can stray from our goal path, as defined in section V. We limited the range of cable lengths for the CDM to between 0 mm and 5 mm to limit the error due to plastic deformation in the cable, as this error increases with an increased bend of the CDM. The 5 mm change in the cable length limits the CDM bending

to a maximum tip-plane angle of 90 degrees with respect to its base-plane. We chose a CDM tip speed limit of 0.5 mm/s, and gain values of $k_p = 0.8$ and $k_d = 0.2$ as defined in section IV.A. These values were chosen based on preliminary path-following tests using a range of values for each of these terms. This particular choice of gains and CDM tip velocity led to the fastest convergence of the CDM tip error. In addition to the objective variables, the RCM was given an allowable error of 2 mm, and the allowable error of the constraint to keep the CDM base axis near the ideal insertion axis was set to 12 degrees. The RCM cylinder's radius was chosen to be 2 mm as the CDM has an outer diameter of 6 mm and the cup's hole has an inner diameter of 10 mm, and the maximum deviation from the ideal insertion axis was chosen to be 12 degrees based on the geometry of the actuation unit.

The paths were each designed as a series of curves that necessitate a range of CDM bending angles to follow and are outside of the workspace possible using a rigid tool in place of the CDM (Figure 9). The first path is a series of 3 curves with a total of 100 waypoints, and the second path is a series of 2 curves with a total of 66 waypoints. The CDM was moved along these paths as the Polaris tracker measured the distance from the CDM marker position to the closest point on the current path. See section IV for a more detailed workflow of the control algorithm. The position of the CDM tip marker was recorded for each iteration of the loop described in section IV, as well as the distance of each recorded point from its respective goal path.

VII. Results

For the assessment of the precision of the CDM tip when following a path (Figure 9), a mean distance from CDM tip to goal path of 0.42 mm was recorded, with a maximum distance of 1.0 mm. A more detailed breakdown of the error mean, maximum, and standard deviation for each trial is shown in Table 1. Using a single-sided t-test on the results of this experiment, we can conclude that CDM tip placement error will not rise above an upper bound of 1 mm with a 95% confidence interval and a p-value less than 0.001.

The first path took an average total of 140 seconds for the CDM to fully traverse, and the second path took approximately 90 seconds to fully traverse. On average, the optimizer needed 4 iterations between motions and each iteration took about 5 ms. This means that we can calculate a new motion approximately every 20 ms. Since the UR5 will be used as a positioning device, the paths were designed to be fully reachable by only rotating the CDM shaft axis and varying its bending angle. During the experiment, there were minimal movements of the UR5 and the CDM was primarily used to achieve the desired CDM tip positions.

The path-following objective was expressed as a series of 3 linear expressions with 7 unknown variables. The joint position and velocity limits, RCM, staying near the ideal axis of entry, and virtual wall constraints were expressed as 46 linear constraints on the minimization of the objective expressions.

VIII. Discussion and Conclusions

With this experiment, we showed that we can effectively use concurrent control of a UR5 and CDM to have the CDM tip reach desired positions within an acetabular cup. Our constrained optimization framework also proved capable of avoiding collisions of the CDM by implementing virtual fixtures.

Although there was a clear source of error due to plastic deformation in the cable, this was to be expected given a static Jacobian function. The shape of the CDM as a function of its cable length differs depending on many factors, some of which change between tests. One important factor is the amount of friction between the CDM and its cable. In fact, a slight bend in the cable can affect the amount of friction present to the point where it changes the CDM shape function. In addition, the experiment used to calculate the Jacobian function represented by J_{CDM} and the CDM shape function are based on an experiment with a CDM that may have different properties than the one used in these experiments. These factors lead us to expect an increase in error when using the CDM within this framework.

Upon closer examination of an instance of the largest CDM tip error (Figure 9) it becomes clear that the CDM is repeatedly bending above and below the path. The largest error in our system is the uncertainty of the CDM shape, and so our largest errors in the experiment are due to improper movements of the CDM. The feedback from the optical tracker is able to guide the CDM tip back onto the goal path, but sometimes it first strays from the path. When larger bending angles of the CDM were required to follow the path this happens more often, as the error in our CDM shape estimation increases with a larger bending angle.

We currently use the Polaris tracker for feedback on the CDM tip location, and future work includes using this to approximate the CDM shape and use it as the input for a dynamically updating Jacobian function [24]. This Jacobian would be much more adept at coming up with a solution specifically catered to the current CDM configuration, and thus would have much lower error and converge more quickly than the open-loop function. The use of an adaptive Jacobian function can also potentially compensate for the errors due to the plastic deformation of the cable, therefore, allowing the CDM to relax the 5-mm cable length range constraint and, therefore, increase the operating workspace.

Acknowledgments

This work is supported by NIH/NIBIB grant R01 EB016703.

References

1. Murphy RJ, Kutzer M, Segreti S, Lucas B, Armand M. Design and kinematic characterization of a surgical manipulator with a focus on treating osteolysis. Robotica. 2014; 32(6):835–850.
2. Kutzer, M., Segreti, S., Brown, C., Taylor, RH., Mears, S., Armand, M. Design of a new cable driven manipulator with a large open lumen: Preliminary applications in the minimally-invasive removal of osteolysis; Proceedings of the 2011 IEEE International Conference on Robotics and Automation (ICRA); May. 2011 p. 2913-2920.
3. Berry DJ. Periprosthetic fractures associated with osteolysis: A problem on the rise. The Journal of Arthroplasty. 2003; 18(3, Supplement 1):107–111. [PubMed: 12730943]

4. Clohisy JC, Calvert G, Tull F, McDonald D, Maloney WJ. Reasons for revision hip surgery: a retrospective review. Clin Orthop Relat Res. Dec.2004 (429):188–192.
5. Dattani R. Femoral osteolysis following total hip replacement. Postgraduate Medical Journal. May; 2007 83(979):312–316. [PubMed: 17488859]
6. Alambeigi, F., Sefati, S., Murphy, RJ., Iordachita, I., Armand, M. Design and characterization of a debriding tool in robot-assisted treatment of osteolysis. IEEE International Conference on Robotics and Automation (ICRA); Stockholm, Sweden. 2016. p. 5664-5669.
7. Alambeigi, F., Wang, Y., Murphy, RJ., Iordachita, I., Armand, M. Toward Robot-Assisted Hard osteolytic Lesion Treatment using a Continuum Manipulator; 2016 38th Annual International Conference of the IEEE Engineering in Medicine and Biology Society; 2016. p. 5103-5106.
8. Alambeigi F, Wang Y, Sefaty S, Gao C, Murphy RJ, Iordachita I, Taylor RH, Armand M. A Curved-Drilling Approach in Core Decompression of the Femoral Head osteonecrosis using a Continuum Manipulator. IEEE Robotics and Automation Letters. 2016 submitted to.
9. Liu, H., Farvardin, A., Pedram, SA., Iordachita, I., Taylor, RH., Armand, M. Large deflection shape sensing of a continuum manipulator for minimally-invasive surgery; Robotics and Automation (ICRA), 2015 IEEE International Conference on; 2015. p. 201-206.
10. Murphy, RJ., Otake, Y., Taylor, RH., Armand, M. Predicting Kinematic Configuration from String Length for a Snake-like Manipulator Not Exhibiting Constant Curvature Bending", in; Intelligent Robots and Systems (IROS), 2014 IEEE/RSJ International Conference on; 2014. p. 3515-3521.
11. Kapoor, A., Li, M., Taylor, RH. Constrained Control for Surgical Assistant Robots. Proc. of the 2006 IEEE International Conference on Robotics and Automation; Orlando, Florida. 2006.
12. Simaan N, Xu Kai, Wei Wei, Kapoor A, Kazanzides P, Taylor R, Flint P. Design and Integration of a Telerobotic System for Minimally Invasive Surgery of the Throat. The International Journal of Robotics Research. 2009; 28(9):1134–1153. [PubMed: 20160881]
13. Kapoor, A., Simaan, N., Taylor, RH. Suturing in confined spaces: constrained motion control of a hybrid 8-DoF robot; Proc. of the 2005 12th IEEE International Conference on Advanced Robotics;
14. Murphy, RJ., Moses, MS., Kutzer, MDM., Chirikjian, GS., Armand, M. Constrained workspace generation for snake-like manipulators with applications to minimally invasive surgery; in Robotics and Automation (ICRA), 2013 IEEE International Conference on; May. 2013 p. 5341-5347.
15. Alambeigi, F., et al. Control of the coupled motion of a 6 DoF robotic arm and a continuum manipulator for the treatment of pelvic osteolysis; Proc. of the 2014 36th International Conference of the IEEE Engineering in Medicine and Biology Society;
16. Universal Robots User Manual, Version 3.0. Universal Robots; Odense, Denmar: 2014. p. I-61
17. Sefati, S., Alambeigi, F., Murphy, R., Iordachita, I., Armand, M. FBG-Based Large Deflection Shape Sensing of a Continuum Manipulator: Manufacturing optimization; Proc. International Conference of the IEEE SENSORS (SENSORS'16); 2016. p. 1511-1513.
18. Liu H, Farvardin A, Grupp R, Murphy RJ, Taylor RH, Iordachita I, Armand M. Shape Tracking of a Dexterous Continuum Manipulator utilizing Two Large Deflection Shape Sensors. The IEEE Sensors Journal. 2015; 15(10):5494–5503. [PubMed: 27761103]
19. Roesthuis R, Sarthak M. Steering of Multisegment Continuum Manipulators using Rigid-Link Modeling and FBG-Based Shape Sensing. IEEE Transactions on Robotics. 2016; 32(2):372–382.
20. Otake Y, Stayman JW, Zbijewski W, Murphy RJ, Kutzer MD, Taylor RH, Siewerdsen JH, Armand M. Model-Based Cone-Beam CT Reconstruction for Image-Guided Minimally Invasive Treatment of Hip osteolysis. Proc. of SPIE. 2013; 8313
21. Polaris Optical Tracking Systems. Northern Digital Inc; Waterloo, Canada: 2013. p. 6
22. Boctor E, Viswanathan A, Choti M, Taylor RH, Fichtinger G, Hager G. A Novel Closed Form Solution for Ultrasound Calibration. Proc. of the 2004 IEEE International Symposium on Biomedical Imaging.
23. Yaniv Z. Which pivot calibration? Proc. of SPIE. 2015; 9415
24. Yip M, Camarillo D. Model-Less Feedback Control of Continuum Manipulators in Constrained Environments. Proc. of the 2014 IEEE Transactions on Robotics.

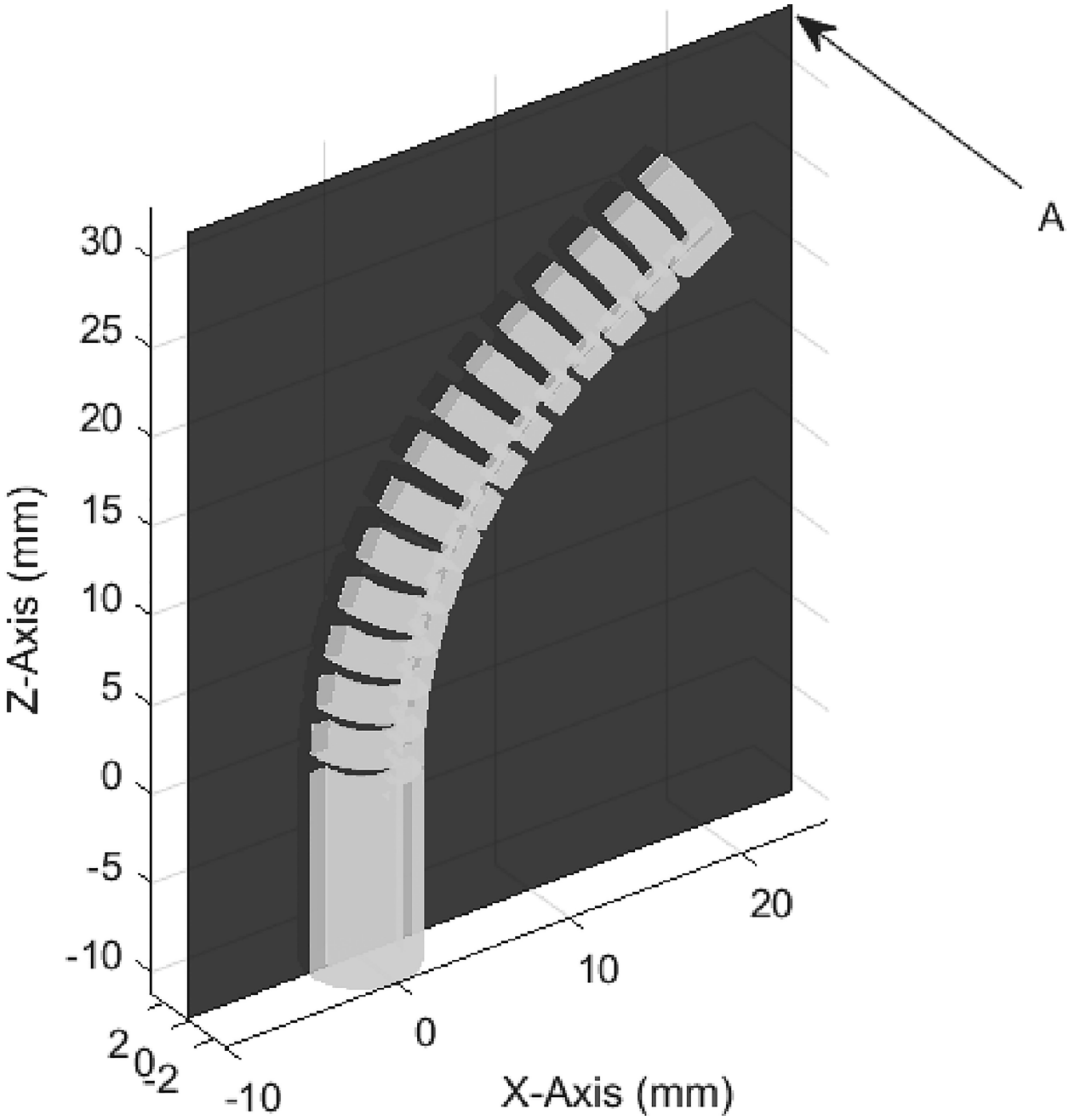

Figure 1.
Diagram of CDM bending with a cable length of 4 mm showing P_{CDM}'s x and z axes. A-Bending plane of the CDM.

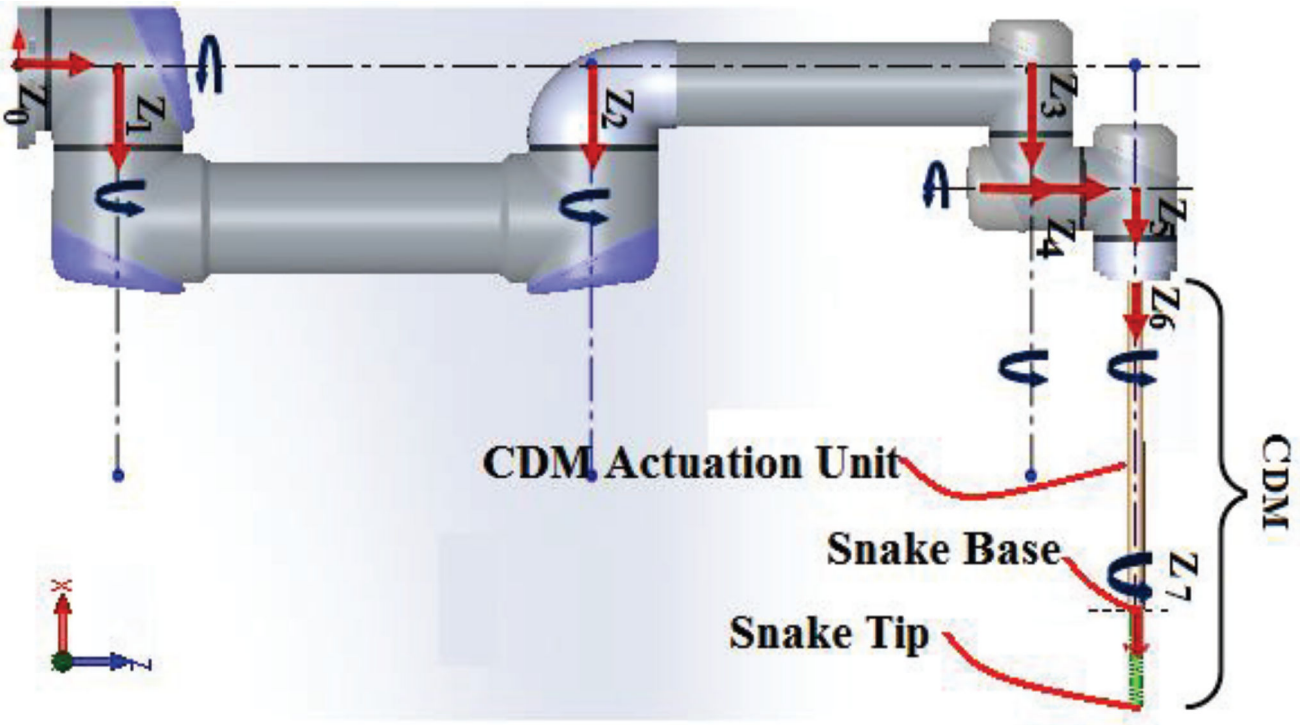

Figure 2.
Joint coordinate frames defined by the coupled D-H parameters.

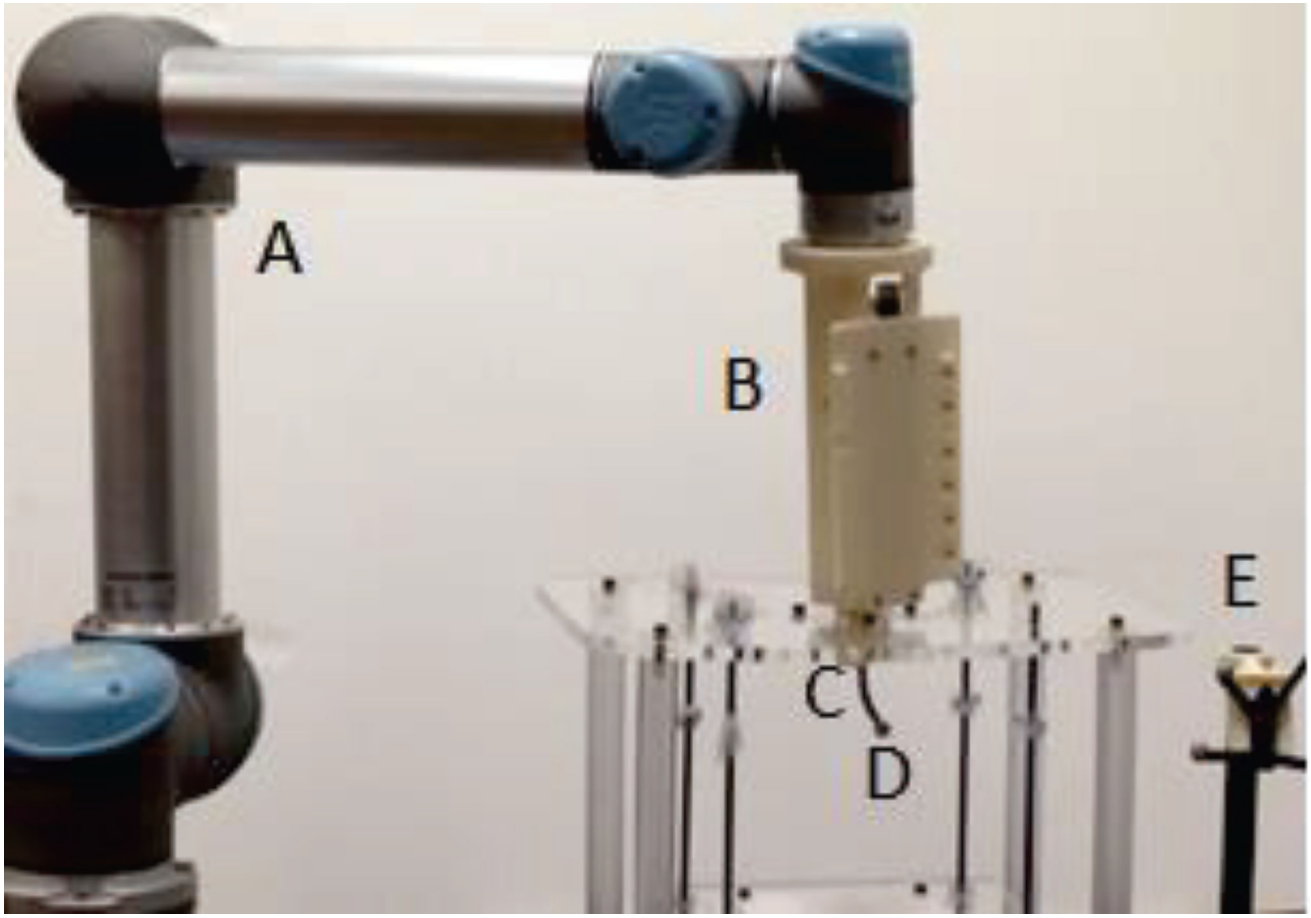

Figure 3.
UR5 with actuation unit mounted to its end effector and CDM inserted. A- UR5 robot arm. B- Actuation unit for controlling CDM motors. C- CDM. D- Optical marker attached to CDM tip for error tracking. E- Reference tool for optical tracker.

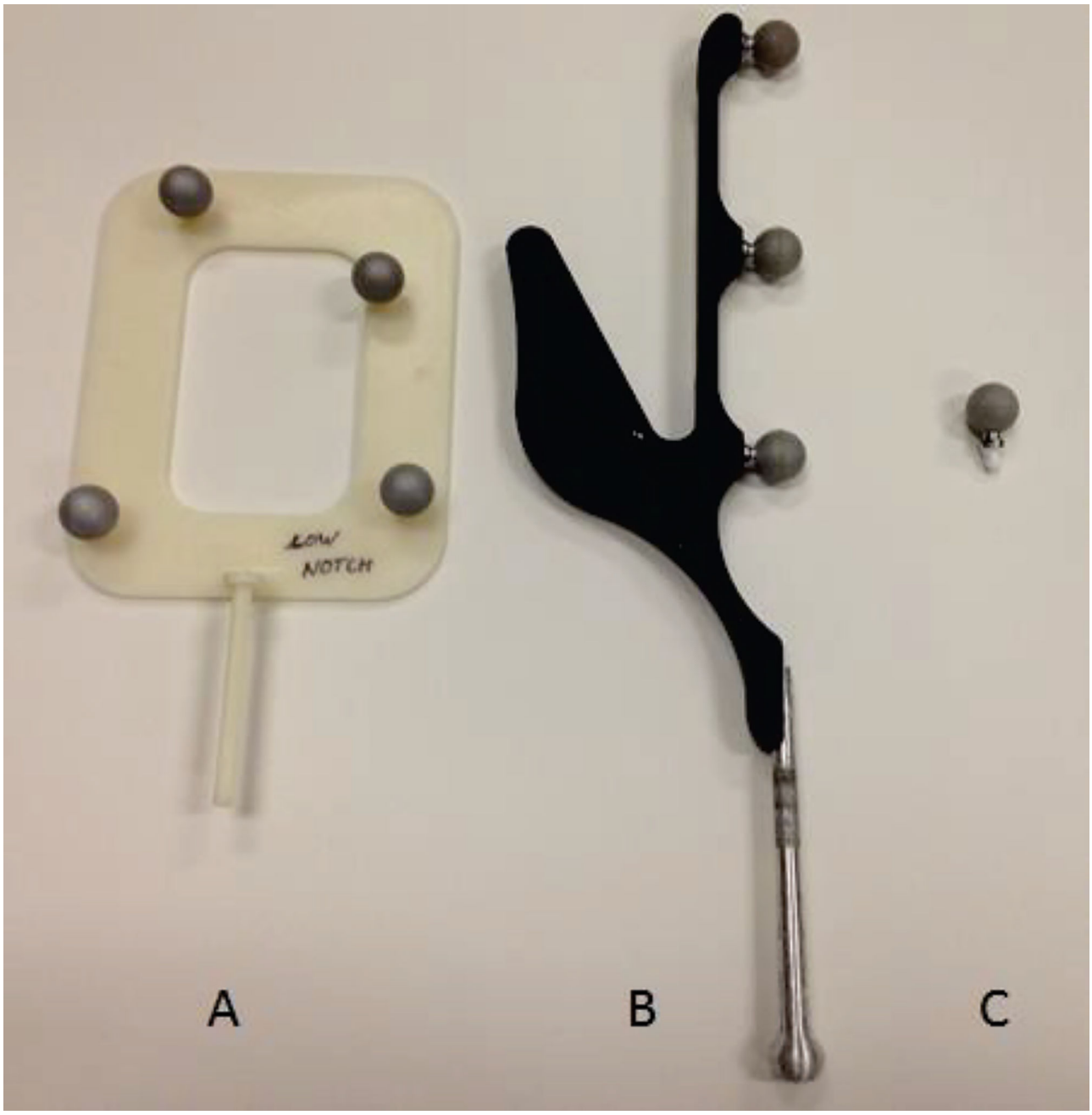

Figure 4.
Calibration tools. A- Calibration jig used for determining CDM tip location. B- Digitizer for determining acetabular cup screwhole center location. C- Adapter for inserting NDI marker into CDM tip.

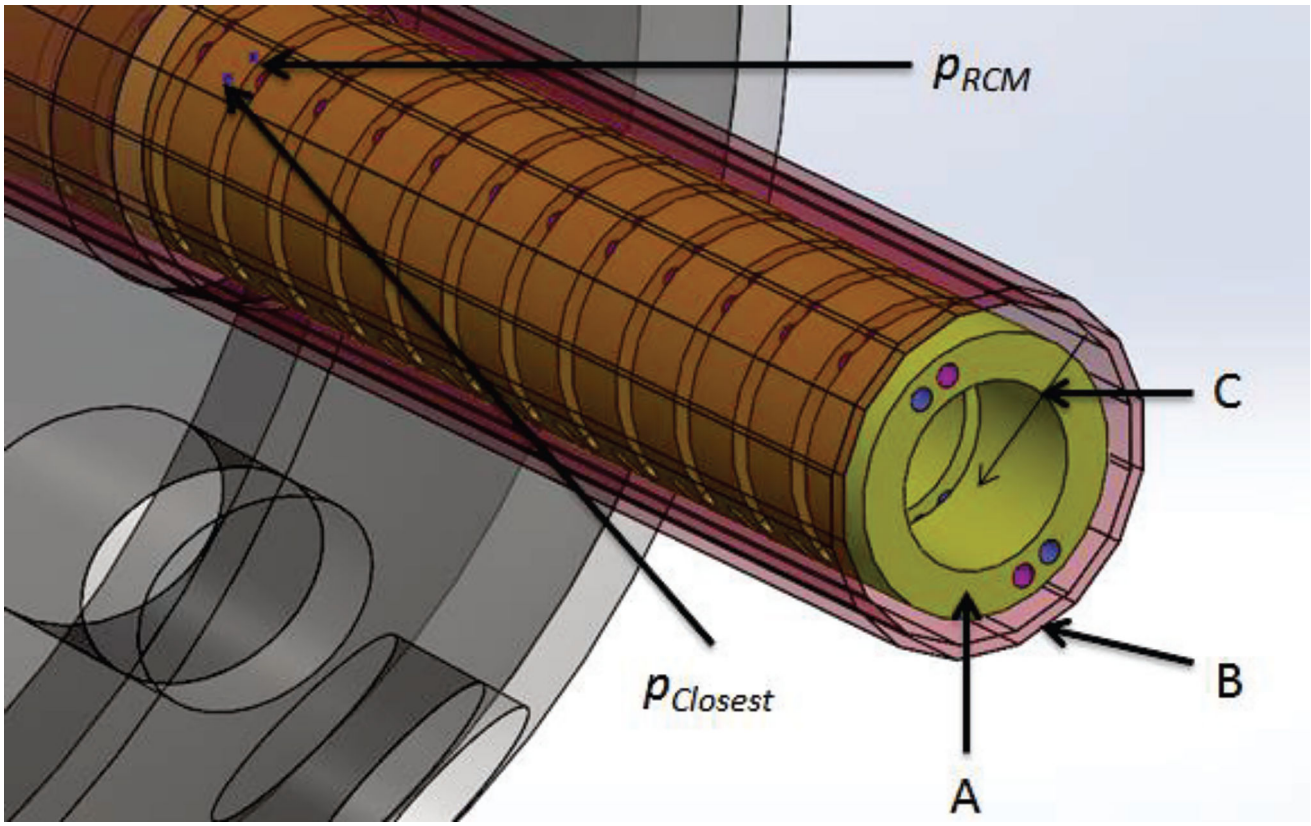

Figure 5.
RCM constraint definition. A- CDM tip. B- Plane barriers on the motion of $p_{Closest}$ approximating a cylinder. C- A normal vector ν_i for one of these planes with magnitude ε.

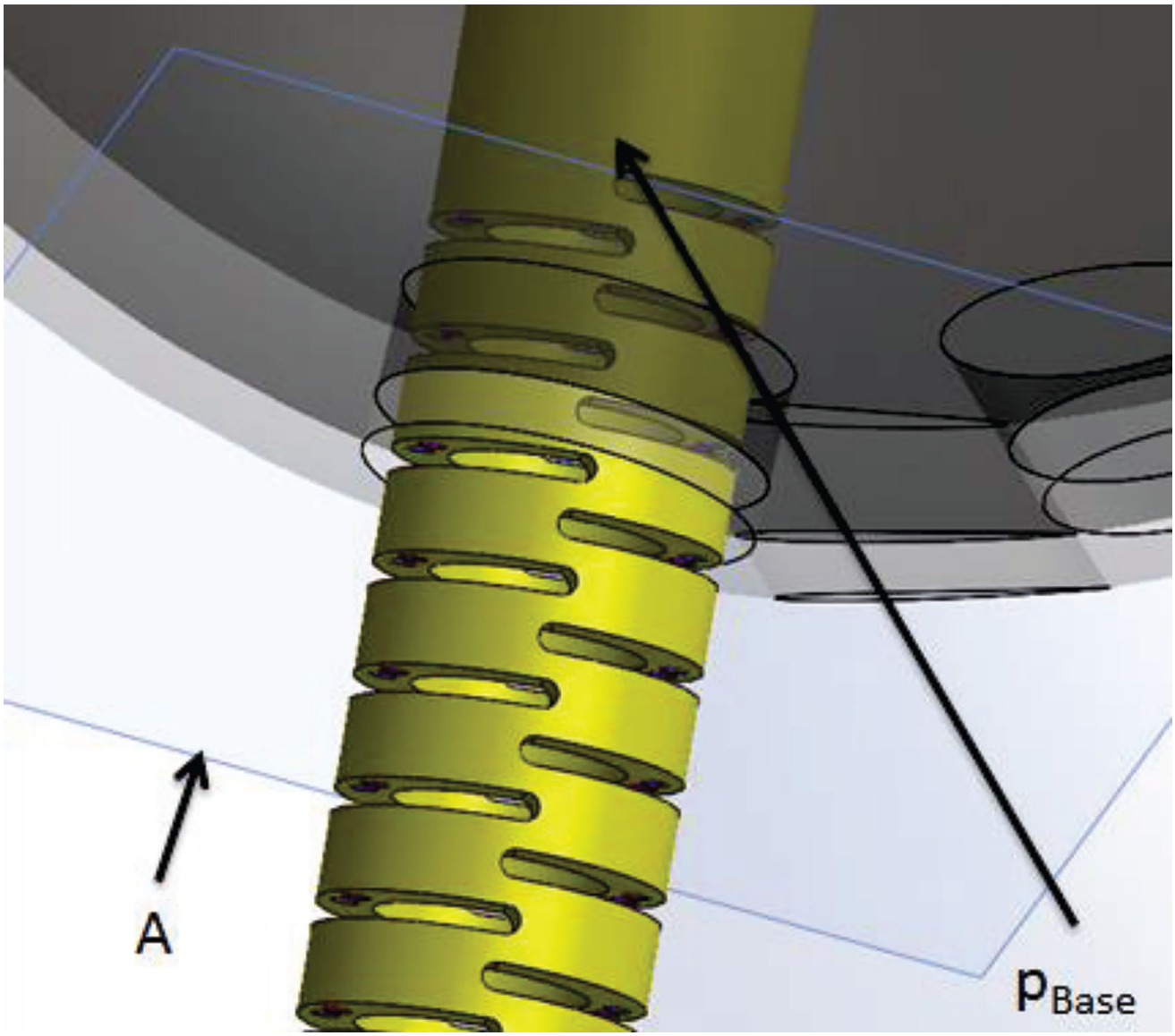

Figure 6.
Visualization of plane used to ensure the entire CDM is within the acetabular cup. A- Plane barrier on the motion of p_{Base}.

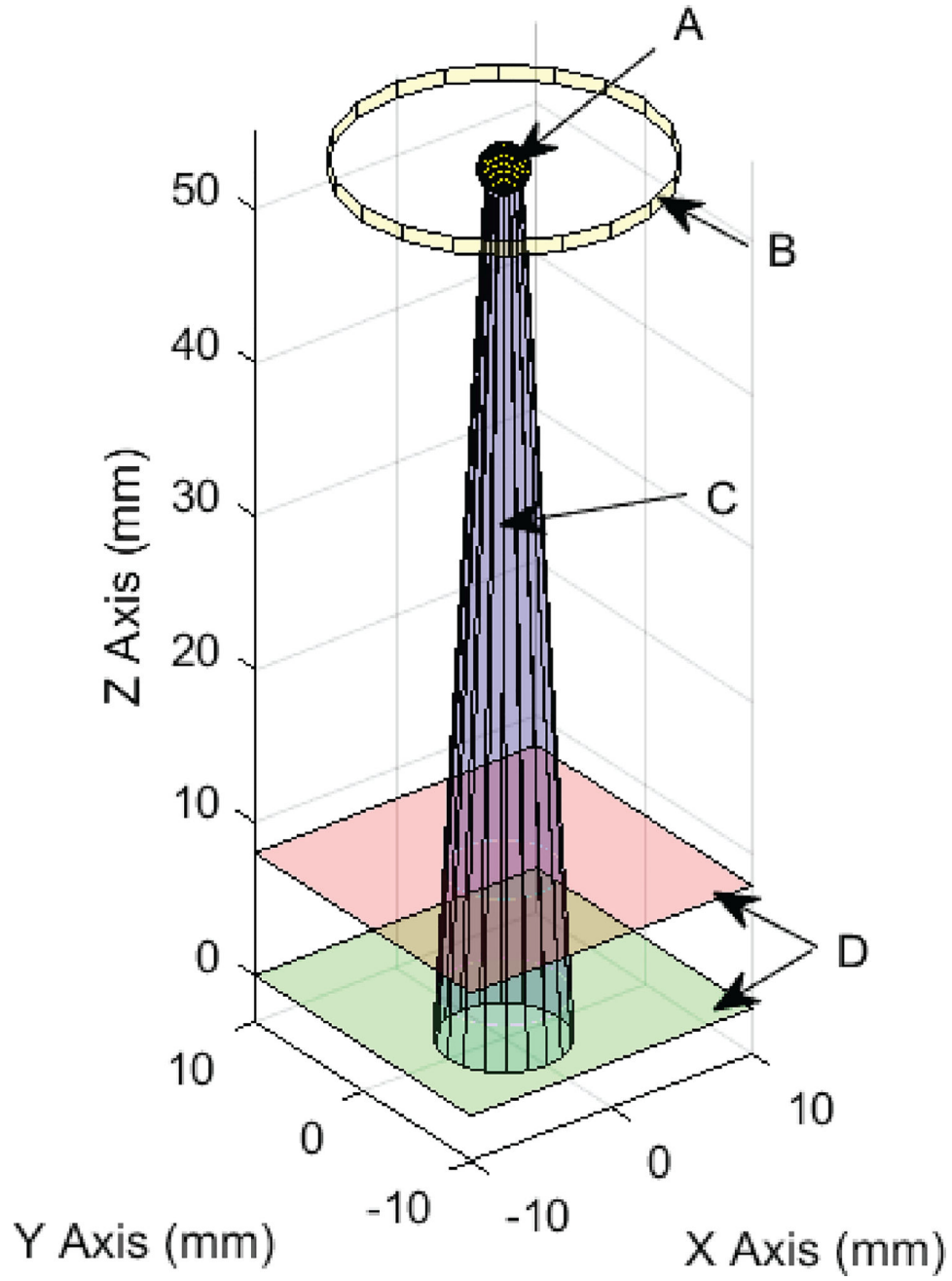

Figure 7.

Workspace of the CDM tip with all constraints enabled. A- Sphere representing the maximum distance the CDM base can stray from the RCM point. B- This ring shows the location of the cup hole. C- This cone shows how the RCM constrains the CDM tip. D- These planes show the virtual wall constraints.

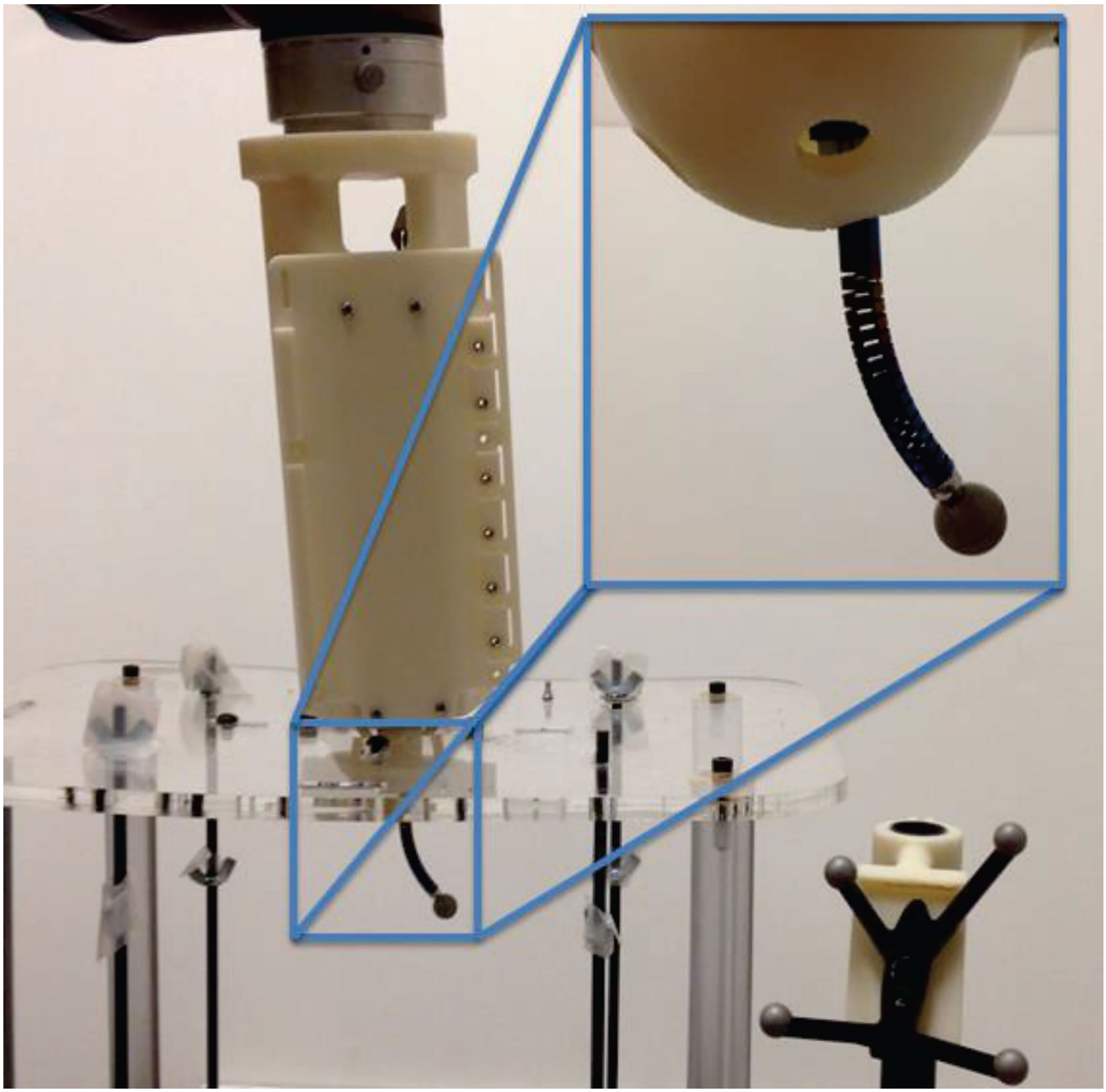

Figure 8.
Experimental setup with the CDM inserted into the actuation unit. Inset: Close-up of the CDM with a Polaris marker attached.

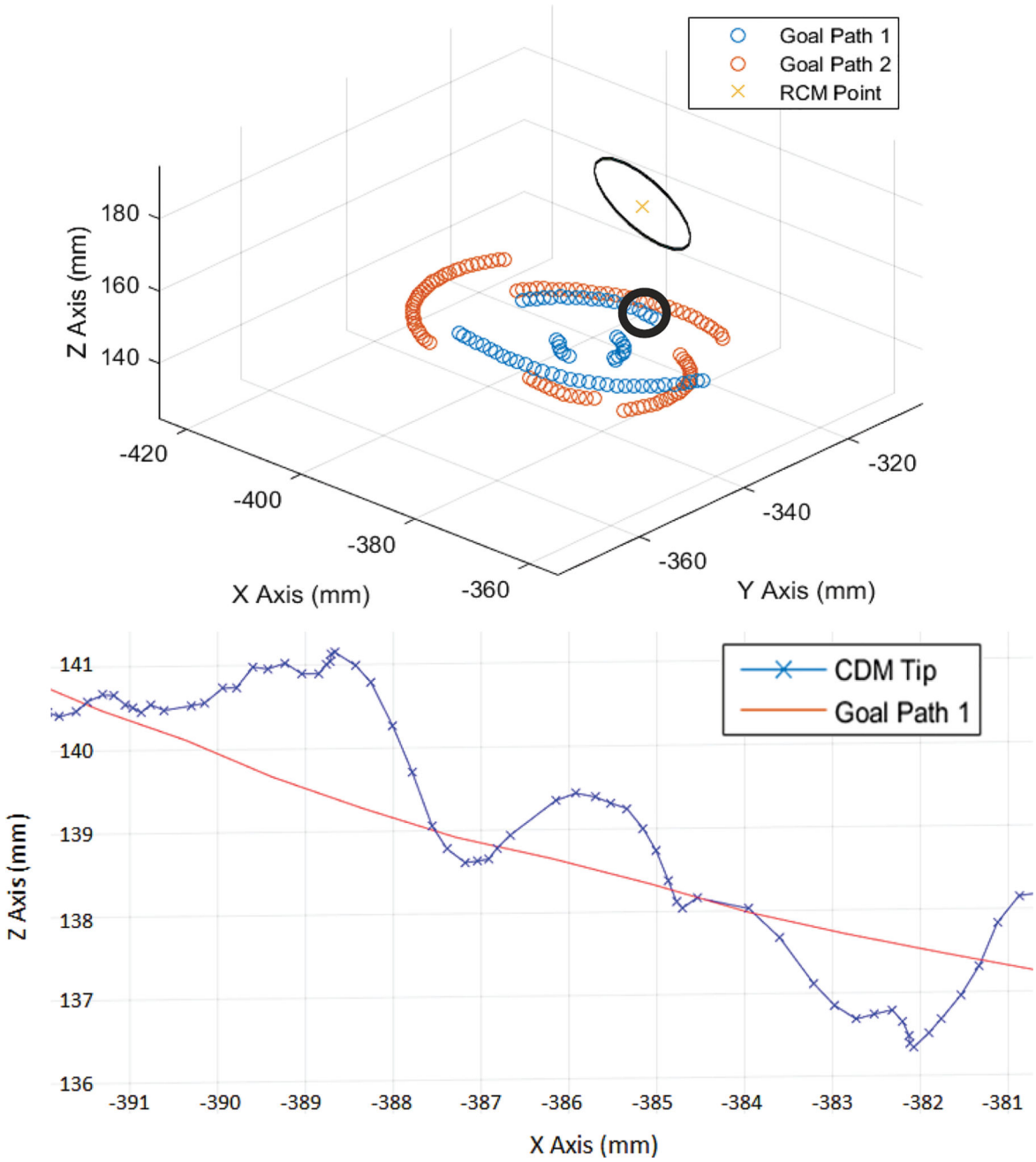

Figure 9.

A- A 3D view showing both goal paths and the location of the cup hole. B- A close-up of part of a path achieved by the CDM tip relative to its goal path. The data used in this figure comes from the circled section of the first trial on the first path in A.

TABLE I

Summary of CDM tip errors from following two paths for multiple trials.

	Path 1		
	Trial 1	Trial 2	Trial 3
Mean Error (mm)	0.46	0.43	0.51
Maximum Error (mm)	1.0	1.0	1.0
Stdev of Error (mm)	0.31	0.28	0.3
	Path 2		
	Trial 1	Trial 2	
Mean Error (mm)	0.34	0.35	
Maximum Error (mm)	1.0	1.0	
Stdev of Error (mm)	0.3	0.29	